J. Fluid Mech. (2022), *vol*. 946, A5, doi:10.1017/jfm.2022.594

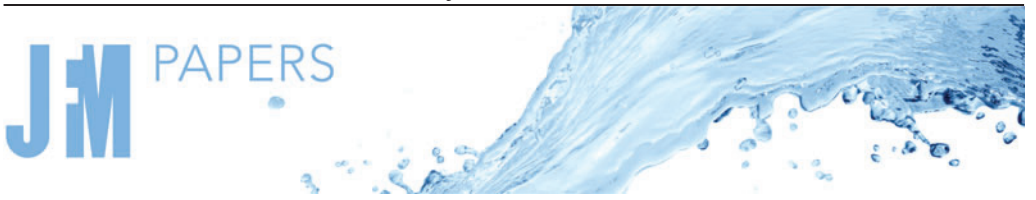

Drag reduction by a flexible hairy coating

Qian Mao[1,2], Jiazhen Zhao[2], Yingzheng Liu[1] and Hyung Jin Sung[2,†]

[1]Key Laboratory of Education Ministry for Power Machinery and Engineering, School of Mechanical Engineering, Shanghai Jiao Tong University, 800 Dongchuan Road, Shanghai 200240, China

[2]Department of Mechanical Engineering, KAIST, 291 Daehak-ro, Yuseong-gu, Daejeon 34141, Korea

(Received 15 December 2021; revised 30 June 2022; accepted 7 July 2022)

The hydrodynamic mechanism of drag reduction by a flexible hairy coating was explored using the penalty immersed boundary method. A two-dimensional flexible hairy coating is constituted by multiple flexible filaments. A simulation of a cylinder without a hairy coating at a Reynolds number of 100 was also performed for comparison. The results of the simulations show good agreement with the experimental data by Niu & Hu (*Phys. Fluids*, vol. 23, 2011, 101701), where maximum drag reduction of 22% was attained at a particular length, bending rigidity, coating density and coating angle of the hairy coating. The hydrodynamic mechanism of drag reduction was characterized in terms of the wake pattern, shape deformation and kinetic energy of the hairy coating. The effect of a non-uniform bending rigidity of the hairy coating on drag reduction was explored. A stable streamline shape of the hairy coating was found to delay the vortex formation and stabilize the recirculation zone, resulting in decreased form drag. Active flapping of the hairy coating with enhanced vortex shedding is adverse to drag reduction. A hairy coating with a stiff base and flexible trailing edge is beneficial to maintaining a stable shape.

Key words: drag reduction

1. Introduction

Vortex shedding in the wake of a bluff body causes cyclic pressure fluctuations, thereby inducing unsteady loads and substantial drag, even leading to vortex-induced vibrations. Passive flow control strategies for suppressing vortex shedding, e.g. installing a rigid or flexible splitter plate behind a bluff body, have received much attention. A rigid splitter plate suppresses vortex shedding by separating shear layers on either side of the wake (Roshko 1955). A flexible splitter plate pushes the vortex downstream and finally stabilizes the wake (Wu *et al.* 2014). In nature, hair, feathers and plants can self-adapt to the surrounding flow (shape self-adaptation or reconfiguration) because of their

† Email address for correspondence: hjsung@kaist.ac.kr

flexibility. The shape self-adaptation under flow in various biological species is beneficial to aero/hydrodynamic performance, increasing speed, reducing energy consumption and drag (Koehl 1984; Bechert *et al.* 2000; De Langre 2008). A bioinspired flexible hairy coating attached to the rear surface of a bluff body has displayed strong potential and high effectiveness in drag reduction. Understanding the hydrodynamic mechanism of drag reduction by a flexible hairy coating is desirable to promote bio-inspired designs.

Extensive attention has been devoted to drag reduction by employing a flexible object, e.g. a flexible plate or filament in a bluff body. Shukla, Govardhan & Arakeri (2013) experimentally investigated the dynamics of a flexible plate attached to a circular cylinder. A flexible plate with an appropriate length was found to effectively suppress vortex shedding, which offsets the fluctuations of separation flow behind a cylinder (Teksin & Yayla 2016; Shen *et al.* 2019). Lee & You (2013) reported that the flexibility of a plate attached to a cylinder adversely modulates drag, the bending rigidity and length of the plate being important parameters for drag reduction. A relatively long plate with low flexibility pushes the vortex downstream and finally stabilizes the wake, demonstrating better drag reduction than a stationary rigid plate (Wu *et al.* 2014). Bagheri, Mazzino & Bottaro (2012) observed that an asymmetric flapping filament reduces drag on a cylinder by breaking the spontaneous symmetry. In addition, two flexible filaments attached to the top and bottom surfaces of a cylinder have been found to effectively reduce drag and lift fluctuations, displaying better drag reduction than a single filament (Deng, Mao & Xie 2019; Banerjee *et al.* 2021). Other simulations involving variations of various parameters (e.g. length of flexible filaments and the attachment angle between two filaments, among others) have been reported (Wu, Wu & Zhan 2016; Abdi, Rezazadeh & Abdi 2019; García-Baena *et al.* 2021). Pertaining to investigations of hairy coatings, Favier *et al.* (2009) numerically studied the flow around a circular cylinder partially coated with articulated short rigid hair; the hairy coating effectively reduced drag and lift fluctuations by stabilizing the wake. In addition, a flexible hairy coating was experimentally studied in a flowing soap film; a flexible hairy coating with an appropriate length and coating area easily self-adapted to the flow, which caused a 'dead water' region and reduced the scale of the wake, resulting in a substantial increase in pressure behind the cylinder (Niu & Hu 2011; Kunze & Brücker 2012). In nature, hair and feathers are known to have non-uniform bending rigidity, with a stiff base and a flexible trailing edge. Few studies of the effects of the magnitude and distribution of the bending rigidity in a hairy coating have been reported.

The aforementioned small-scale experiments in a flowing soap film encounter some limitations, such as requiring continuous changes of the bending rigidity of a hairy coating. As an alternative, numerous versions of the immersed boundary (IB) method have been developed to simulate flow–flexible-body interaction problems (Huang, Shin & Sung 2007; Huang & Sung 2010; Chen *et al.* 2020). Recently, Mao *et al.* (2021*a*) simulated a rigid plate (normal to the oncoming flow) with a trailing closed filament acting as a flexible afterbody; substantial drag reduction was achieved via the shape deformation of the flexible afterbody. The flexible afterbody shows limited shape self-adaptation; for example, it cannot streamline its body because of the incompressibility and pressure difference between its interior and exterior. The underlying mechanism of interaction by a flexible hairy coating was resolved using the penalty IB method, enabling reproduction of the experimental data of Niu & Hu (2011) for comparison. The influence of a flexible hairy coating on drag reduction has not yet been fully elucidated and warrants a more detailed investigation.

The objective of the present study was to explore the drag variation of a cylinder with a flexible hairy coating by using the penalty IB method, in an effort to reveal

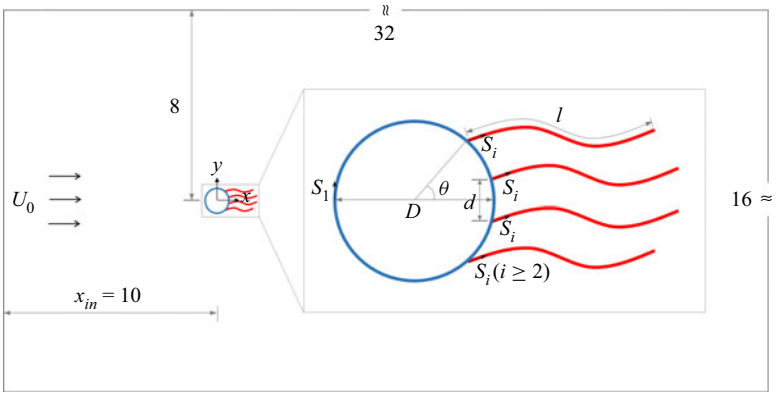

Figure 1. Schematic of a cylinder with a flexible hairy coating.

the hydrodynamic mechanism of drag reduction. A flexible hairy coating is constituted by multiple flexible filaments. A simulation of a cylinder without a hairy coating at a Reynolds number of 100 was also performed for comparison. We examined drag variations of such a cylinder–hair system by varying the length (l), bending rigidity (γ), distance between adjacent filaments (d) and coating angle (θ) of the hairy coating and comparing the results with the experimental data reported by Niu & Hu (2011). The hydrodynamic mechanism of drag reduction was characterized in terms of the wake pattern and shape deformation of the hairy coating. A stable streamline shape of the hairy coating that results in minimum drag was identified. The effect of the non-uniform bending rigidity of the hairy coating on drag reduction was explored.

2. Computational model

2.1. *Problem formulation*

A schematic of a cylinder with a flexible hairy coating in the computational domain is shown in figure 1. The flexible hairy coating is constituted by multiple flexible filaments, which are symmetrically arranged on the rear surface of the cylinder. The diameter of the cylinder and the length of the flexible filaments are D and l, respectively. The fluid motion is defined on a fixed uniform Eulerian grid, where x and y represent the streamwise and spanwise directions, respectively. The computational domain is 32 in length ($-10 \leq x \leq 22$) and 16 in height ($-8 \leq y \leq 8$). The cylinder is pinned at $x = 0$ and symmetric to $y = 0$. Parameter d is the distance between adjacent filaments, and θ denotes the angle between the root of the outermost filament and $y = 0$. The motions of flexible filaments are defined on moving Lagrangian grids under curvilinear coordinate system s_i ($i \geq 2$), whereas s_1 is fixed. At the inlet, the uniform streamwise velocity ($U_0 = 1$), zero spanwise velocity ($v = 0$) and zero pressure gradient ($\partial p/\partial x = 0$) were applied. Free-stream conditions ($u = 1$, $v = 0$) were imposed at the top and bottom boundaries. At the outlet, a convective boundary condition was specified (Huang *et al.* 2007; Hwang *et al.*, 2016; Hwang & Sung, 2018). The penalty IB method (Peskin 2002; Huang *et al.* 2007) was used.

The incompressible viscous flow is governed by the Navier–Stokes (N–S) equation and the continuity equation, which are dimensionless

$$\frac{\partial \boldsymbol{u}}{\partial t} + \boldsymbol{u} \cdot \nabla \boldsymbol{u} = -\nabla p + \frac{1}{Re} \nabla^2 \boldsymbol{u} + \sum \boldsymbol{f}_j, \tag{2.1}$$

$$\nabla \cdot \boldsymbol{u} = 0, \tag{2.2}$$

where $\boldsymbol{u}$ is the velocity vector, p is the pressure and $\boldsymbol{f}_j$ denotes the feedback momentum force to enforce the no-slip condition along the IB. Here, j is the index number, where $j = 1$ and $j \geq 2$ represent a cylinder and flexible filaments, respectively. The Reynolds number is $Re = \rho_0 U_0 D/\mu$, where ρ_0 and μ are the fluid density and the dynamic viscosity, respectively. Equations (2.1) and (2.2) were non-dimensionalized using the following characteristic scales: the reference cylinder diameter D for the length, U_0 for the velocity, D/U_0 for the time, $\rho_0 U_0^2$ for the pressure and $\rho_0 U_0^2/D$ for the feedback momentum force $\boldsymbol{f}_j$. For convenience, the dimensionless quantities are written in the same form as their dimensional counterparts.

A cylinder ($j = 1$) is pinned at $x = 0$ and symmetric to $y = 0$. The position of the cylinder ($\boldsymbol{X}_1 = (X_1(s_1), Y_1(s_1))$) is expressed by

$$X_1(s_1) = \frac{D}{2}\cos\left(2\pi\frac{s_1}{\pi D}\right), \tag{2.3}$$

$$Y_1(s_1) = \frac{D}{2}\sin\left(2\pi\frac{s_1}{\pi D}\right), \tag{2.4}$$

where s_1 ranges from 0 to πD. In the present study, the flexible filaments ($j \geq 2$) are massless and inextensible. The movement of the filaments is governed by the motion equation and the inextensibility condition, which are dimensionless

$$\frac{\partial^2 \boldsymbol{X}_j}{\partial t^2} = \frac{\partial}{\partial s_j}\left(\sigma\frac{\partial \boldsymbol{X}_j}{\partial s_j}\right) - \frac{\partial^2}{\partial s_j^2}\left(\gamma\frac{\partial^2 \boldsymbol{X}_j}{\partial s_j^2}\right) - \boldsymbol{F}_j + \boldsymbol{F}_{cj}, \tag{2.5}$$

$$\frac{\partial \boldsymbol{X}_j}{\partial s_j} \cdot \frac{\partial \boldsymbol{X}_j}{\partial s_j} = 1, \tag{2.6}$$

where s_j ($j \geq 2$) ranges from 0 to l, $\boldsymbol{X}_j = (X_j(s_j, t), Y_j(s_j, t))$ is the position, σ is the tension force along the flexible filaments' axis, γ is the bending rigidity, $\boldsymbol{F}_j = (F_{xj}(s_j), F_{yj}(s_j))$ denotes the Lagrangian forcing exerted on the flexible filaments by the surrounding fluid and $\boldsymbol{F}_{cj} = (F_{cxj}(s_j), F_{cyj}(s_j)))$ denotes the repulsive force between adjacent filaments. Equations (2.5) and (2.6) have been non-dimensionalized using the following characteristic scales: D for the length, D/U_0 for the time, $\rho_1 U_0^2/D$ for the Lagrangian forcing $\boldsymbol{F}_j$ and repulsive force $\boldsymbol{F}_{cj}$, $\rho_1 U_0^2$ for the tension force σ and $\rho_1 U_0^2 D^2$ for the bending rigidity γ. Parameter ρ_1 denotes the density difference between the flexible filament and the surrounding fluid. For convenience, the dimensionless quantities are written in the same form as their dimensional counterparts.

In the present study, the tension force σ is determined by the constraint of inextensibility and is a function of s_j and t (Huang *et al.* 2007), whereas the bending rigidity γ is assumed to be constant (uniform) or is a function of s_j (non-uniform). In the present study, the uniform bending rigidity varies in the range $0.002 \leq \gamma \leq 0.015$.

The fixed ends ($s_j = 0$) of the flexible filaments are attached to the cylinder, and a clamped boundary condition is applied

$$\left.\begin{aligned} Y_j(0) &= d(j-2) - d(N-1)/2, \\ X_j(0) &= \sqrt{(D/2)^2 - Y_j(0)^2}, \\ \frac{\partial \boldsymbol{X}}{\partial s_j} &= (1, 0) \quad \text{at } s_j = 0, \end{aligned}\right\} \tag{2.7}$$

where N is the number of the flexible filaments. At the free ends ($s_j = l$) of the flexible filaments, we have

$$\sigma = 0, \quad \frac{\partial^2 \boldsymbol{X}_j}{\partial s_j^2} = (0, 0), \quad \frac{\partial^3 \boldsymbol{X}_j}{\partial s_j^3} = (0, 0). \tag{2.8}$$

A virtual stiff spring with damping was used to strongly connect the boundary of the structure to a massless boundary. The interaction force (Lagrangian forcing $\boldsymbol{F}_j$) between the fluid and the IB can be calculated by the feedback law (Goldstein, Handler & Sirovich 1993)

$$\boldsymbol{F}_j = \alpha \int_0^t (\boldsymbol{U}_{ibj} - \boldsymbol{U}_j)\, \mathrm{d}t' + \beta(\boldsymbol{U}_{ibj} - \boldsymbol{U}_j), \tag{2.9}$$

where α and β are large negative free constants (Shin, Huang & Sung 2008), $\boldsymbol{U}_{ibj}$ ($j \geq 1$) is the fluid velocity obtained by interpolation at the IB and $\boldsymbol{U}_j$ ($j \geq 1$) is the velocity of the structure expressed by $\boldsymbol{U}_j = \mathrm{d}\boldsymbol{X}_j/\mathrm{d}t$ ($\boldsymbol{U}_j = 0$ for a cylinder). The total drag (F_d) is the sum of F_{xj} (i.e. $F_d = \sum F_{xj}$).

Transformation between the Eulerian and Lagrangian variables can be realized by the Dirac delta function (Peskin 2002). The velocity $\boldsymbol{U}_{ibj}$ obtained by interpolation across the position of the structure $\boldsymbol{X}_j$ is expressed as

$$\boldsymbol{U}_{ibj}(s_j, t) = \int_\Omega \boldsymbol{u}(\boldsymbol{x}, t)\ \delta(\boldsymbol{X}_j(s_j, t) - \boldsymbol{x})\, \mathrm{d}\boldsymbol{x}, \tag{2.10}$$

where Ω denotes the fluid domain. The Eulerian momentum force $\boldsymbol{f}_j$ obtained by spreading the Lagrangian forcing $\boldsymbol{F}_j$ to the nearby Eulerian grids is expressed as

$$\boldsymbol{f}_j(\boldsymbol{x}, t) = \rho \int_\Gamma \boldsymbol{F}_j(s_j, t)\ \delta(\boldsymbol{x} - \boldsymbol{X}_j(s_j, t))\, \mathrm{d}s, \tag{2.11}$$

where $\rho = \rho_1/(\rho_0 D)$ arises from non-dimensionalization and Γ is the structure domain.

The repulsive force $\boldsymbol{F}_{cj}$ is used to handle collisions between adjacent filaments. Owing to fluid lubrication, the filaments do not actually collide but rather interact repulsively via the intervening fluid when they are in close proximity to each other (Glowinski *et al.* 1999; Huang *et al.* 2007). Without this force, the filaments may intersect, or even overlap with each other. The short-range repulsive force can be formulated using the Dirac delta function

$$\boldsymbol{F}_{cj}(s_j, t) = \int_0^l \delta(\boldsymbol{X}_j(s_j, t) - \boldsymbol{X'}_j(s'_j, t)) \frac{\boldsymbol{X} - \boldsymbol{X'}}{|\boldsymbol{X} - \boldsymbol{X'}|}\, \mathrm{d}s', \tag{2.12}$$

where $\boldsymbol{X}_j(s_j, t)$ and $\boldsymbol{X'}_j(s'_j,\ t)$ are the position vectors along the two adjacent filaments, respectively. The kinetic energy E_k is defined by

$$E_k = \int_\Gamma 0.5 \rho U_{ib}^2\, \mathrm{d}s. \tag{2.13}$$

Details regarding the discretization of the governing equations and numerical method can be found in the works of Park & Sung (2001), Huang *et al.* (2007) and Lee *et al.* (2014).

	Δx	$\bar{C}_D$	C'_L	St
Present work	1/32	1.396	0.346	0.167
Present work	1/64	1.405	0.348	0.167
Yuan *et al.* (2014)	1/40	1.397	0.338	0.160
Shin *et al.* (2008)	1/64	1.440	0.350	0.168
Xu & Wang (2006)	1/20	1.423	0.340	0.171

Table 1. Simulation data for a cylinder without a flexible hairy coating.

	Domain	Δx	x_{in}	$\bar{C}_D$	C'_L	St
Present work	16×8	1/32	4	1.568	0.404	0.183
	32×16	1/32	4	1.517	0.391	0.175
	32×16	1/32	8	1.415	0.378	0.167
	32×16	1/32	10	1.396	0.346	0.167
	32×16	1/32	12	1.397	0.351	0.167
	32×32	1/32	12	1.382	0.356	0.167
	64×16	1/32	10	1.398	0.350	0.167

Table 2. Domain test for a cylinder without a flexible hairy coating.

2.2. *Numerical validation*

We first simulated flow over a cylinder without a flexible hairy coating. Re was set at 100 on the basis of U_0 and D. Uniform grids were used in the present study. The number of Lagrangian points along the cylinder was 201 ($\Delta l \approx 1/64$). The present results, including the averaged drag coefficient $\bar{C}_D$, the lift coefficient fluctuations C'_L and the Strouhal number St, are compared with the results of other simulations (Xu & Wang 2006; Shin *et al.* 2008; Yuan *et al.* 2014) in table 1; good agreement is observed. Table 2 shows the results of the domain test. The result of 32×16 agrees well with those of 32×32 and 64×16. The result of $x_{in} = 10$ agrees well with that of $x_{in} = 12$. Finally, a grid resolution of $\Delta x = 1/64$, a domain size of 32×16 and $x_{in} = 10$ were selected to improve the accuracy of the present simulation.

For further validation, we conducted simulations of a cylinder with a flexible hairy coating ($l/D = 2.0$, $\gamma = 0.002$, $D/d = 4$, $\theta = 48.6^\circ$). A time step of $\Delta t = 0.0003$ was chosen in the present study to ensure stability and convergence. The maximum Courant number was approximately 0.05. Several trial calculations were repeated to determine the sensitivity of the results. Figure 2(a) shows the time histories of drag coefficient C_D for three grid resolutions of filaments ($\Delta l = 1/32$, 1/64, 1/128). The result of $\Delta l = 1/64$ agrees well with that of $\Delta l = 1/128$. The grid resolution of $\Delta l = 1/64$ for the structure was chosen to ensure a sufficiently high accuracy of the simulation. An initial development of C_D is shown in figure 2(b), where the pattern starts to be periodic after $t \geq 180$ for gathering and averaging data.

3. Results and discussion

We first examine the drag variation of a cylinder with a flexible hairy coating by varying the length (l/D) of the filaments ($D/d = 4$, $\theta = 48.6^\circ$) in figure 3(a). The experimental data of Niu & Hu (2011) are included for comparison; the distance (d) between adjacent filaments and the coating angle (θ) in this previous study are similar to those in the

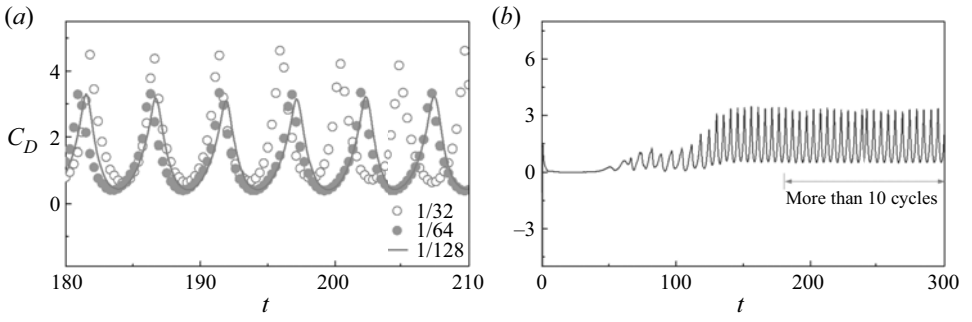

Figure 2. (*a*) Time histories of the drag coefficient (C_D) for different grid resolutions. (*b*) Initial development of C_D.

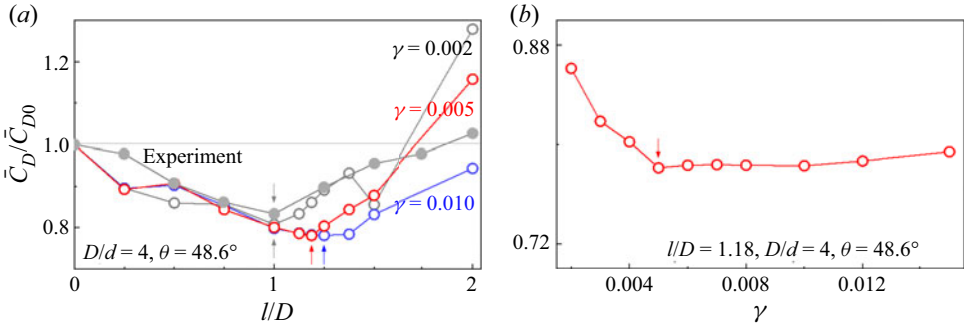

Figure 3. (*a*) Averaged drag coefficients $\bar{C}_D/\bar{C}_{D0}$ as a function of l/D with different bending rigidities γ; (*b*) $\bar{C}_D/\bar{C}_{D0}$ as a function of γ for $l/D = 1.18$ ($D/d = 4$, $\theta = 48.6°$).

present simulation. Here, $\bar{C}_D$ is the averaged drag coefficient for $l/D > 0$ and $\bar{C}_{D0}$ is that for $l/D = 0$. The similarity between the present simulation data and the experimental data is an exciting result; $\bar{C}_D/\bar{C}_{D0}$ decreases and then increases with increasing l/D, showing $\bar{C}_D/\bar{C}_{D0} < 1$ when $l/D \leq 1.75$. This result means that drag reduction is achieved using a flexible hairy coating behind a cylinder. In particular, the minimum $\bar{C}_D/\bar{C}_{D0}$ is attained at $l/D = 1.00$ in the experiment and at $l/D = 1.00$, 1.18, 1.25 in the simulations (corresponding to bending rigidity $\gamma = 0.002$, 0.005, 0.010, respectively). The value of l/D of the minimum point increases with increasing γ. Note that the minimum $\bar{C}_D/\bar{C}_{D0}$ decreases with increasing γ from 0.002 to 0.005, while a slight difference is realized between $\gamma = 0.005$ and 0.010. This result indicates that a critical γ exists for drag reduction. Beyond the minimum point, $\bar{C}_D/\bar{C}_{D0}$ increases rapidly, especially for smaller γ, i.e. the hairy coating is softer. For $l/D > 1.75$, drag even increases ($\bar{C}_D/\bar{C}_{D0} > 1$) compared with that of a cylinder without a hairy coating.

We further examine the effect of γ on $\bar{C}_D/\bar{C}_{D0}$ at $l/D = 1.18$ ($D/d = 4$, $\theta = 48.6°$) in figure 3(*b*). $\bar{C}_D/\bar{C}_{D0}$ decreases with increasing γ until the critical point ($\gamma = 0.005$). For $\gamma > 0.005$, $\bar{C}_D/\bar{C}_{D0}$ slowly increases with increasing γ; i.e. $\bar{C}_D/\bar{C}_{D0}$ is almost insensitive to γ. This result is analogous to obtaining the same minimum $\bar{C}_D/\bar{C}_{D0}$ for $\gamma = 0.005$ and 0.010 in figure 3(*a*). A flexible hairy coating with appropriate length and relatively high bending rigidity more efficiently reduces drag.

On the basis of the critical bending rigidity $\gamma = 0.005$ and the corresponding hairy coating length $l/D = 1.18$, we further explore the effects of the coating density D/d and

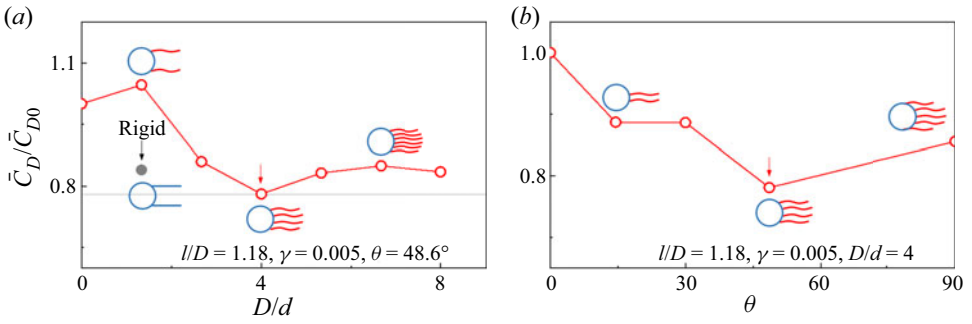

Figure 4. Value of $\bar{C}_D/\bar{C}_{D0}$ as a function of (a) the coating density D/d and (b) the coating angle θ for $l/D = 1.18$ and $\gamma = 0.005$.

the coating angle θ on $\bar{C}_D/\bar{C}_{D0}$ in figure 4. Here, both $D/d = 0$ and $\theta = 0$ represent a cylinder without a hairy coating. In figure 4(a), D/d is varied by adding filaments between the two outermost filaments at $\theta = 48.6°$, i.e. $D/d = (N-1)/\sin\theta$. For $D/d = 1.33$, the value of $\bar{C}_D/\bar{C}_{D0}$ increases compared with its value for $D/d = 0$. Thereafter, $\bar{C}_D/\bar{C}_{D0}$ rapidly decreases and then slowly increases with increasing D/d as a whole. In particular, the minimum $\bar{C}_D/\bar{C}_{D0}$ is attained at $D/d = 4$. In the study of Assi, Bearman & Kitney (2009), the minimum drag is obtained for a freely rotating cylinder with two parallel rigid plates; $\bar{C}_D/\bar{C}_{D0}$ of a cylinder with two parallel rigid filaments is shown in figure 4(a). The flexible hairy coating with appropriate density shows better drag reduction than the parallel rigid plates. In figure 4(b), θ is varied by installing different numbers of filaments behind a cylinder at $D/d = 4$, i.e. $\theta = \arcsin((N-1)d/D)$. The value of $\bar{C}_D/\bar{C}_{D0}$ decreases and then increases with increasing θ; the minimum $\bar{C}_D/\bar{C}_{D0}$ is attained at $\theta = 48.6°$. In sum, drag reduction is accomplished using a flexible hairy coating with appropriate l/D, γ, D/d and θ. An in-depth analysis is needed to elucidate the underlying mechanism of drag reduction of a flexible hairy coating.

3.1. *Flow pattern*

Figure 5 shows the instantaneous contours of vorticity ω_z for different l/D ratios ($\gamma = 0.005$, $D/d = 4$, and $\theta = 48.6°$). For $l/D = 0$ in figure 5(a), alternating clockwise and counterclockwise vortices are shed from the upper and lower sides of the body, near the rear surface of the cylinder. The wake pattern is known as the '2S' mode (Williamson & Govardhan 2004). As l/D increases to 1.18 in figure 5(b), the hairy coating maintains a symmetrical configuration. The symmetrical hairy coating prevents the interaction of shear layers in either side of the wake, leading to a delay of vortex formation. Some vortices that shed from the cylinder are cancelled by mixing with opposite vorticity in the 'coupling region' between the wake and the potential outer flow (Roshko 1955). Only approximately one half of the vorticity that is generated from the cylinder goes into individual vortices, the rest being cancelled by mixing with opposite vortices in the coupling region (Fage & Johansen 1928). The delay of vortex formation weakens ω_z in the extended coupling region before new vortices are generated. Accordingly, a substantially weakened ω_z is observed compared with that corresponding to $l/D = 0$, leading to the drag reaching a minimum at $l/D = 1.18$. As l/D increases further to 2.00 in figure 5(c), the hairy coating is substantially deformed. The further increase in l/D causes active flapping of the hairy

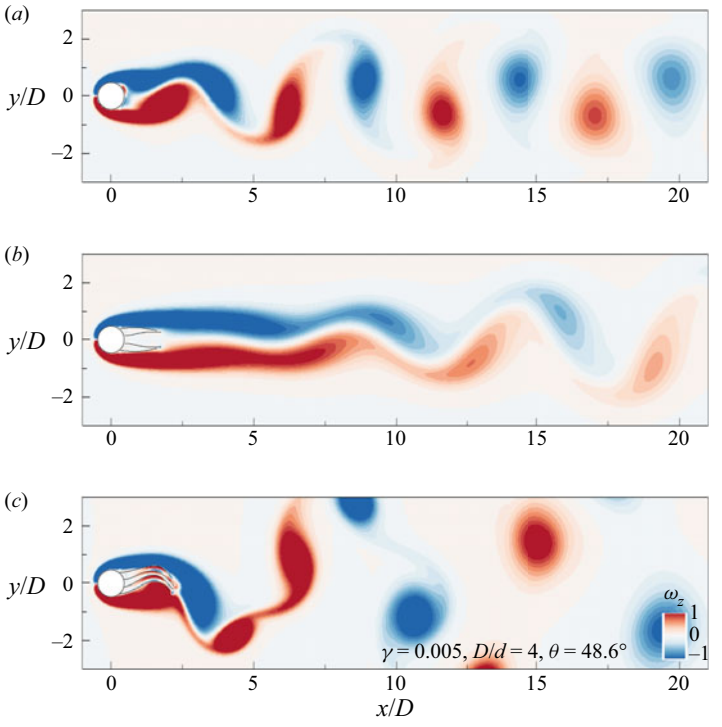

Figure 5. Contours of ω_z for different l/D ($\gamma = 0.005$, $D/d = 4$, and $\theta = 48.6°$): (*a*) $l/D = 0$, (*b*) $l/D = 1.18$ and (*c*) $l/D = 2.00$.

coating, which enhances ω_z with an enlarged wake scale, leading to increased drag. Vortex shedding is effectively suppressed by the hairy coating at $l/D = 1.18$.

Figure 6 shows the contours of time-averaged p and reverse-flow intermittency ($\bar{I}$) for different l/D ($\gamma = 0.005$, $D/d = 4$, and $\theta = 48.6°$). Here, $\bar{I}$ is defined as the proportion of reserve flow over the entire period; $\bar{I} = 1$ and 0 indicate that the fluid always flows upstream and downstream, respectively (Mao *et al.* 2021*b*). The fluid is in an unstable reversal state if $\bar{I}$ is approximately 0.5. As shown in figure 6(*a*), the variation of the negative pressure induced by varying l/D is consistent with the variation of ω_z in figure 5. A negative pressure near the rear surface of the cylinder is observed at $l/D = 0$; this negative pressure is caused by the formation of vortex. The main form drag is caused by the negative pressure behind the cylinder. For $l/D = 1.18$, the hairy coating effectively weakens the negative pressure, leading to a minimum drag. As l/D is increased to 2.00, however, the negative pressure becomes more pronounced, matching even that of $l/D = 0$. Furthermore, the hairy coating shows great effectiveness on the recirculation zone in figure 6(*b*). For $l/D = 0$, an unstable reverse-flow region with green colour ($\bar{I} \approx 0.5$) occupies more than half of the recirculation zone. As the l/D ratio increases to 1.18, the hairy coating lengthens and narrows the recirculation zone, resulting in a stable recirculation zone. This phenomenon has been termed 'direct opposition control' by Pastoor *et al.* (2008). The enlarged recirculation zone with low velocity induces the increase of pressure behind the cylinder. As the l/D ratio increases further to 2.00, the recirculation zone is entirely classified as an unstable reverse-flow region, which corresponds to the active flapping with an enlarged wake scale in figure 5(*c*). Notably, the recirculation zone width ($w/D = 0.83$) of the bare cylinder is similar to that of the hairy

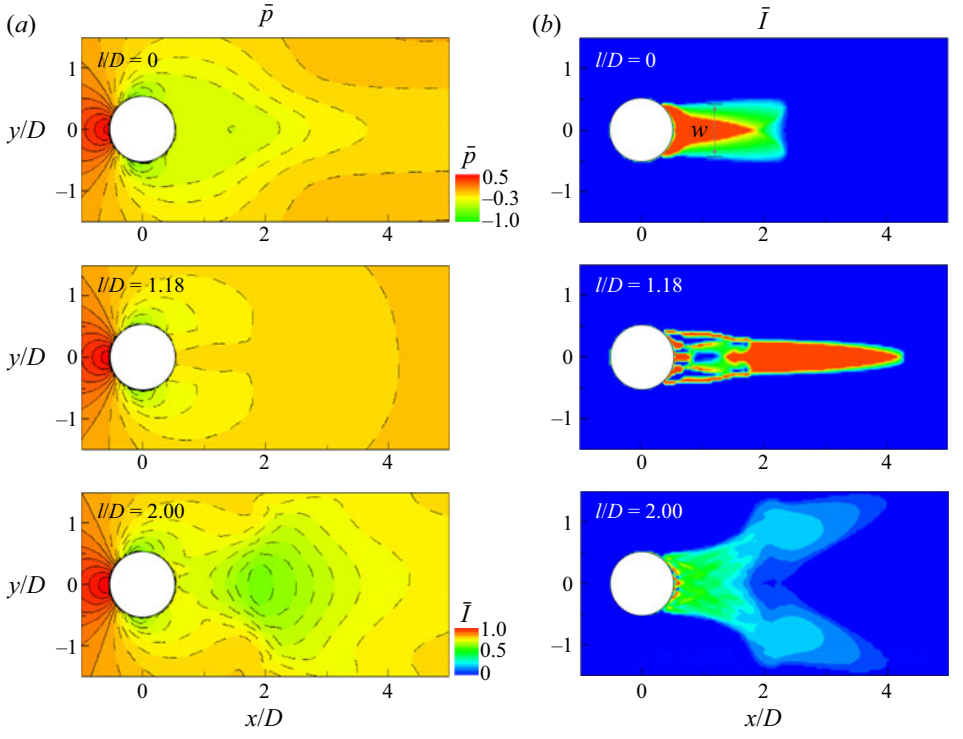

Figure 6. Contours of (*a*) time-averaged pressure and (*b*) reverse-flow intermittency for different l/D ($\gamma = 0.005$, $D/d = 4$ and $\theta = 48.6°$).

coating ($w/D = 0.81$) with optimal coating angle ($\theta = 48.6°$). An appropriate coating angle is beneficial to stabilizing the wake. The further increase in θ with more filaments even causes increased skin frictional drag (Favier *et al.* 2009; Niu & Hu 2011).

To quantitatively examine the delayed vortex formation and increased p at $l/D = 1.18$, the distributions of $\bar{p}$ along the wake ($y = 0$) are displayed in figure 7 for different l/D ($\gamma = 0.005$, $D/d = 4$ and $\theta = 48.6°$). Each pressure curve starts from the rear surface of the cylinder, which undergoes both decreasing and increasing periods, showing $\bar{p} < 0$ as a whole. For $l/D = 0$ in figure 7(*a*), a pressure 'valley' (minimum pressure $\bar{p}_{min}$) is observed downstream of the cylinder, which represents the region of vortex formation (Roshko 1955). The $\bar{p}_{min}$ occurs approximately one diameter downstream of the rear surface of the cylinder ($D_1 = 0.9D$). As l/D increases to 1.18 in figure 7(*b*), the pressure valley disappears, accompanied by a substantial increase in pressure. The $\bar{p}_{min}$ occurs at $D_1 = 1.3D$, indicating a delayed vortex formation compared with that of $l/D = 0$. The hairy coating stabilizes the recirculation zone, which decouples the flow in the hairy coating from the surrounding flow, resulting in a 'dead water' region with low speed (Niu & Hu 2011). The pressure near the rear surface of the cylinder increases because of the delay of vortex formation (increase of D_1) and the formation of 'dead water' (increase of $\bar{p}_{min}$), leading to decreased form drag at $l/D = 1.18$. As the value of l/D increases further to 2.00, an extended length of the hairy coating induces the delay of vortex formation; however, the value of $\bar{p}_{min}$ substantially decreases, as shown in the inset of figure 7. This behaviour is mainly attributable to the active flapping, which significantly enhances ω_z, as shown in figure 5(*c*).

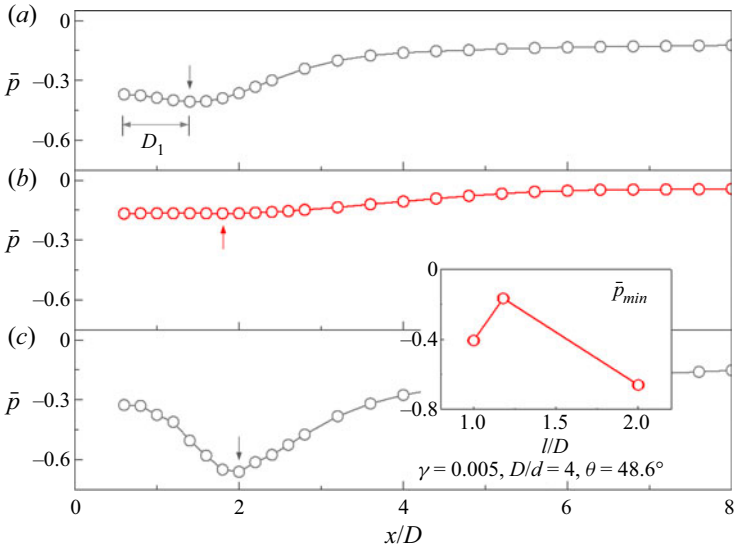

Figure 7. Averaged pressure along the wake ($y = 0$) for different l/D ($\gamma = 0.005$, $D/d = 4$ and $\theta = 48.6°$): (*a*) $l/D = 0$, (*b*) $l/D = 1.18$ and (*c*) $l/D = 2.00$.

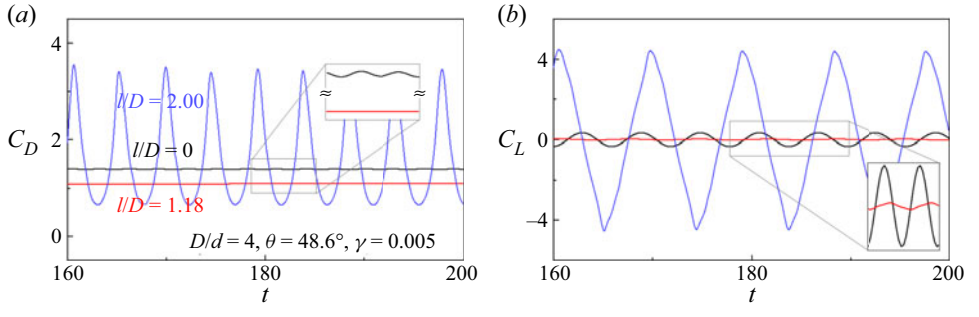

Figure 8. Time histories of (*a*) drag coefficients C_D and (*b*) lift coefficients C_L for different l/D ratios at $\gamma = 0.005$, $D/d = 4$ and $\theta = 48.6°$.

Figure 8 shows the time histories of C_D and C_L for different l/D ($\gamma = 0.005$, $D/d = 4$ and $\theta = 48.6°$). The hairy coating at $l/D = 1.18$ substantially weakens the fluctuations of periodic vortex-induced loads, especially C_D. This result is mainly attributable to the delay of vortex formation, i.e. the region with strong pressure fluctuations remains away from the rear surface of the cylinder. As the l/D ratio increases to 2.00, active flapping of the hairy coating enhances the vortex shedding, resulting in a substantial increase in drag and in the lift fluctuations. The flexible hairy coating for $l/D = 1.18$, $\gamma = 0.005$, $D/d = 4$ and $\theta = 48.6°$ effectively stabilizes the wake. Further analysis pertaining to the shape deformation of the hairy coating for different geometric parameters is needed.

3.2. *Shape deformation*

Figure 9 shows the superposition of instantaneous shapes for different l/D ($\gamma = 0.005$, $D/d = 4$ and $\theta = 48.6°$). A transition of the shape deformation is observed. For $l/D = 0.50$, hairy coating flaps under the vortex shedding, without disturbance between four

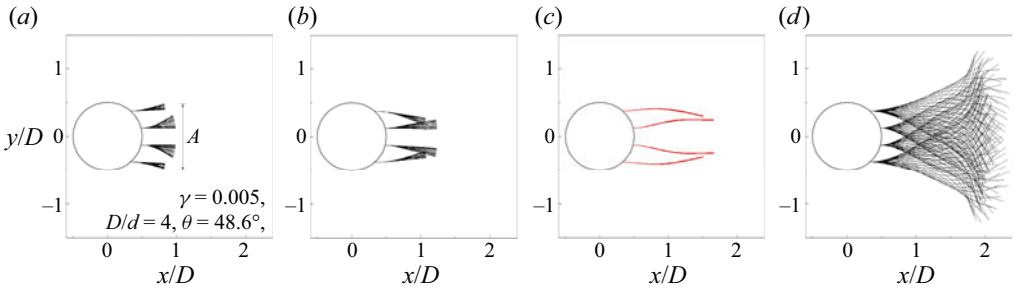

Figure 9. Instantaneous shapes of the hairy coating for different l/D ($\gamma = 0.005$, $D/d = 4$ and $\theta = 48.6°$): (*a*) $l/D = 0.50$, (*b*) $l/D = 0.75$, (*c*) $l/D = 1.18$ and (*d*) $l/D = 2.00$.

filaments because of the short hairy coating. As the l/D ratio increases to 0.75, the outermost filaments bend inward because of the surrounding flow, which decreases the distance between adjacent filaments, leading to collisions among the filaments. As mentioned in § 2.1, two filaments do not actually collide but rather interact (collision force $\boldsymbol{F_c}$) via the intervening fluid when they are in close proximity to each other. The flapping amplitude of filaments for $l/D = 0.75$ is smaller than that for $l/D = 0.50$ because of the collisions. As the l/D ratio increases to 1.18, the interaction between adjacent filaments is enhanced further, leading to a substantial weakening of flapping. The tail of the hairy coating bends inward because of the surrounding flow, resulting in a stable streamline shape. Such a stable structure weakens vortex shedding and leads to a stable recirculation zone, as shown in figures 5 and 6, resulting in minimum drag at $l/D = 1.18$. As the l/D ratio increases further to 2.00, an extended length of the hairy coating induces active flapping, which dominates vortex shedding, leading to an enhanced ω_z with an enlarged wake scale.

To elucidate the shape deformation of the hairy coating in greater detail, the averaged flapping amplitude $\bar{A}$ and kinetic energy $\bar{E}_k$ as a function of l/D ($D/d = 4$ and $\theta = 48.6°$) are shown in figure 10 (E_k is defined in § 2.1). Both $\bar{A}$ and $\bar{E}_k$ first increase and then undergo decreasing and increasing phases with increasing l/D, irrespective of γ. The first increase of $\bar{A}$ and $\bar{E}_k$ corresponds to the 'flapping regime' in figure 9(*a*). The filaments do not disturb each other because of the short hairy coating. Parameters $\bar{A}$ and $\bar{E}_k$ increase with increasing l/D in this regime. The decrease of $\bar{A}$ and $\bar{E}_k$ corresponds to the 'suppressed flapping regime' in figure 9(*b*). A longer hairy coating is easier to deform, leading to an interaction between adjacent filaments, resulting in decreases in $\bar{A}$ and $\bar{E}_k$. In addition, a 'weak flapping regime' with a stable streamline shape (figure 9*c*) is obtained at $\bar{E}_k \approx 0$, as shown in figure 10(*b*). The second increase of $\bar{A}$ and $\bar{E}_k$ corresponds to the 'active flapping regime' in figure 9(*d*). The further increase in l/D breaks a stable state of the hairy coating. Note that a hairy coating with a lower γ exhibits higher $\bar{A}$ and $\bar{E}_k$ values as a whole, corresponding to greater drag in figure 3. In addition, the second decrease of $\bar{A}$ and $\bar{E}_k$ for $\gamma = 0.002$ at $l/D = 1.5$ is caused by the asymmetric flapping of the hairy coating, which leads to decreased drag, as shown in figure 3(*a*), because of the weakened wake (Bagheri *et al.* 2012; Mao *et al.* 2021*a*). $\bar{A}$ and $\bar{E}_k$ significantly increase at $l/D = 2.0$ (not shown here).

Parameters $\bar{A}$ and $\bar{E}_k$ are further examined as functions of D/d and θ ($l/D = 1.18$ and $\gamma = 0.005$) in figure 11. The variations of $\bar{A}$ and $\bar{E}_k$ are consistent with the drag variation in figure 4. As shown in figure 11(*a*), $\bar{A}$ and $\bar{E}_k$ decrease and then increase with increasing D/d (i.e. a decreased space between adjacent filaments). The decreased space induces an

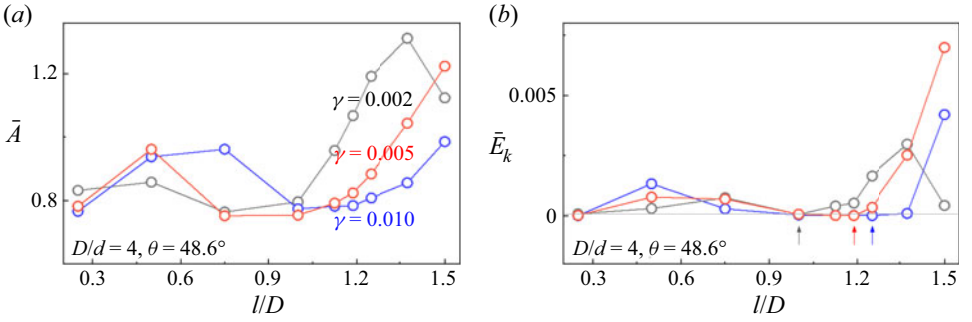

Figure 10. Averaged (*a*) flapping amplitude $\bar{A}$ and (*b*) kinetic energy $\bar{E}_k$ as functions of l/D for different γ ($D/d = 4$ and $\theta = 48.6°$).

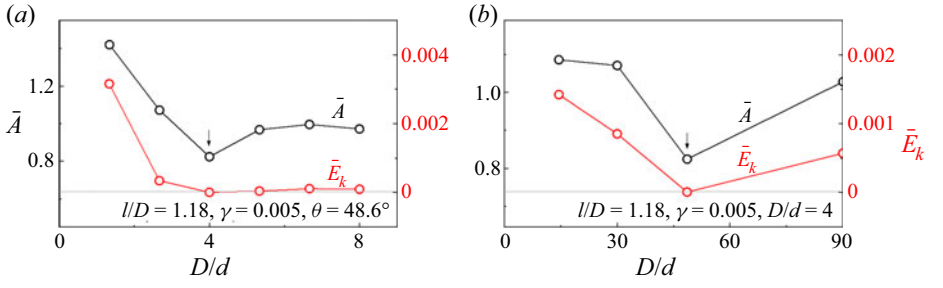

Figure 11. Values of $\bar{A}$ and $\bar{E}_k$ as functions of (*a*) D/d and (*b*) θ for $l/D = 1.18$ and $\gamma = 0.005$.

interaction among the filaments, enhancing a stable hair coating. For $D/d > 4$, a further decreased space is ineffective, i.e. $\bar{A}$ and $\bar{E}_k$ are insensitive to D/d. The stability of the hairy coating reaches a critical value at $D/d = 4$, leading to low drag and a low $\bar{E}_k$. As shown in figure 11(*b*), minimum $\bar{A}$ and $\bar{E}_k$ values are obtained at $\theta = 48.6°$. The distance between the bases of the outermost filaments ($w/D = 0.81$) is similar to the width of the recirculation zone ($w/D = 0.83$) in figure 6(*b*), leading to a stable hairy coating ($\bar{E}_k \approx 0$). The further increase in θ results in the outside filaments being placed in a high-speed surrounding flow, which in turn results in an increase in $\bar{E}_k$. In sum, a stable hairy coating is beneficial to drag reduction.

To elucidate the flapping dynamics in the flapping regime, the time histories of C_L, E_k and the transverse position of the tail-point (y_t) and mid-point (y_m) of the hairy coating are shown in figure 12(*a*) for $l/D = 2.00$, $\gamma = 0.005$, $D/d = 4$ and $\theta = 48.6°$. The y_t and y_m values are calculated on the basis of the averaged transverse position of the tail-point and mid-point of four filaments, respectively. The vorticity contours corresponding to moments $\boldsymbol{A} - \boldsymbol{C}$ in figure 12(*a*) are shown in figure 12(*b*).

The hairy coating reaches its upstroke extreme at moment $\boldsymbol{A}$, corresponding to local minimum E_k and maximum y_t. A positive vortex is formed at the lower side of the hairy coating because of the transverse flapping motion, resulting in a local minimum C_L. The hairy coating moves downward under the effect of the local minimum hydrodynamic force, accompanied by an increase in E_k and a decrease in y_t. The hydrodynamic force does positive work on the hairy coating. At moment $\boldsymbol{B}$, the hairy coating reaches its mid-position with local maximum E_k and $C_L \approx 0$. Substantial deformation of the hairy coating is observed at this moment. A negative vortex shed from the upper side of the hairy

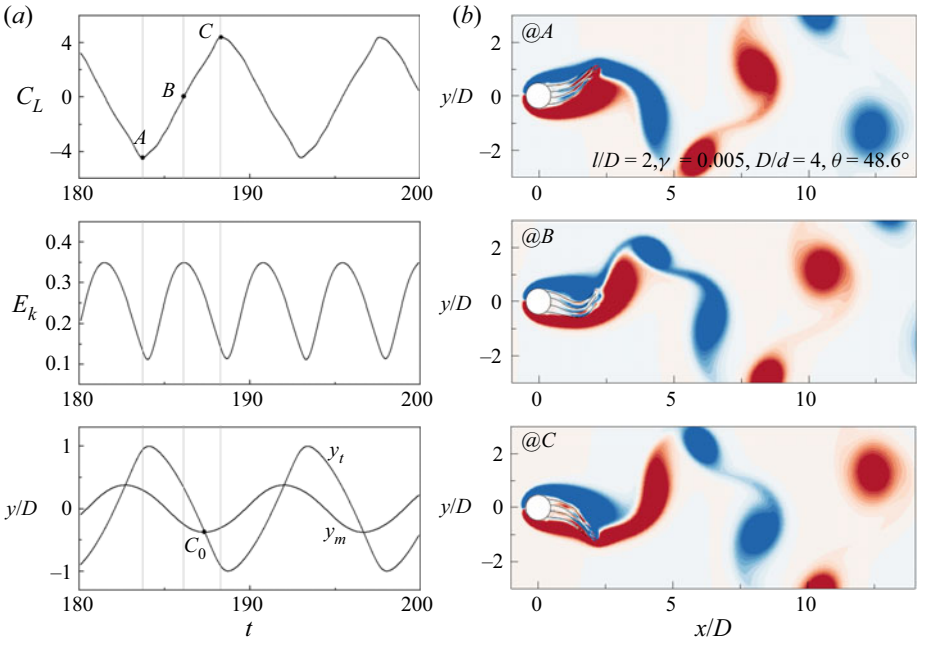

Figure 12. (*a*) Time histories of C_L, E_k and the transverse positions of the tail-point (y_t) and mid-point (y_m) of the hairy coating. (*b*) Instantaneous vorticity contours at *A*, *B* and *C* for $l/D = 2.00$ ($\gamma = 0.005$, $D/d = 4$ and $\theta = 48.6°$).

coating is formed, resulting in a deceleration of the hairy coating in the region $\boldsymbol{B} - \boldsymbol{C}$. Note that y_m reaches a local minimum at moment $\boldsymbol{C}_0$, earlier than y_t. This result means that the movement of the tail shows hysteresis relative to the movement of the main body of the hairy coating. In the region $\boldsymbol{C}_0 - \boldsymbol{C}$, the trailing edge of the hairy coating moves downward under the effect of the inertial force, inducing the division of two vortices. At moment $\boldsymbol{C}$, a negative vortex is formed at the upper side of the hairy coating, resulting in a local maximum C_L. The hairy coating reaches its downstroke extreme with local minimum E_k and y_t.

Figure 13 shows $\bar{C}_D/\bar{C}_{D0}$ as a function of Re ($50 \leq Re \leq 175$); $\bar{C}_D/\bar{C}_{D0}$ decreases with increasing Re until $Re = 100$ and is insensitive to Re for $Re \geq 100$. The experimental data of Niu & Hu (2011) at $Re = 8000$ are included for comparison. A small difference in $\bar{C}_D/\bar{C}_{D0}$ (less than 5%) is observed despite a large difference in Re. The superpositions of instantaneous shapes for $Re = 100$ and 175 are plotted in the inset; the hairy coating in the 'weak flapping regime' maintains a stable shape by the interaction between adjacent filaments.

3.3. *Non-uniform bending rigidity*

Hair and feathers are known to have non-uniform bending rigidity, with a stiff base and flexible trailing edge. We further examine $\bar{C}_D/\bar{C}_{D0}$ as a function of the bending rigidity gradient k in figure 14 ($l/D = 1.18$, $D/d = 4$ and $\theta = 48.6°$). Non-uniform bending rigidity γ_{si} is defined as $\gamma_{si} = k(s_i - l/2) + 0.005$ ($0 \leq s_i \leq l$) to ensure that $\bar{\gamma}_{si} = 0.005$, as shown in figure 14(*a*). For comparison, the data for uniform bending rigidity $\gamma = 0.005$ are included. As shown in figure 14(*b*), the most dramatic drag reduction is observed in the

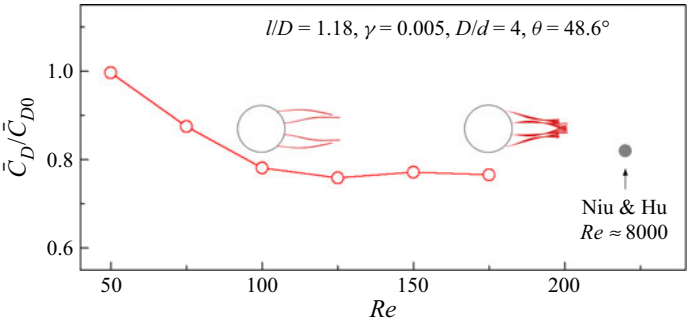

Figure 13. Value of $\bar{C}_D/\bar{C}_{D0}$ as a function of Re for $l/D = 1.18$, $\gamma = 0.005$, $D/d = 4$ and $\theta = 48.6°$.

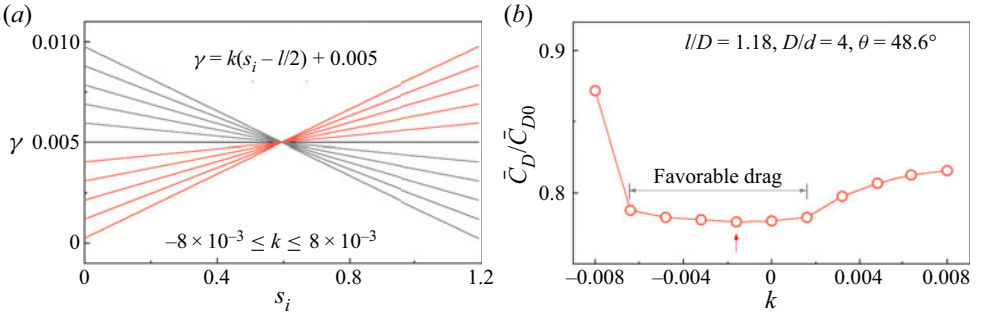

Figure 14. (*a*) The distributions of γ along the hairy coating; (*b*) $\bar{C}_D/\bar{C}_{D0}$ as a function of k for $l/D = 1.18$ ($D/d = 4$ and $\theta = 48.6°$).

region $-4.8 \times 10^{-3} \leq k \leq 1.6 \times 10^{-3}$, which is referred to here as the 'favourable drag zone'. Drag increases rapidly when k is beyond the favourable drag zone. In particular, a minimum drag is attained at $k = -1.6 \times 10^{-3}$. The favourable drag zone is mainly located in the region of negative k, indicating that the hairy coating with a stiff base and flexible trailing edge is beneficial to drag reduction.

Figure 15 shows the variations of $\bar{A}$ and $\bar{E}_k$ as a function of k ($l/D = 1.18$, $D/d = 4$ and $\theta = 48.6°$). Two different regions are defined by $\bar{E}_k$: the 'weak flapping region' (corresponding to the favourable drag zone) and the 'active flapping region'. The hairy coating belongs to an active flapping region when k is greater than $k = 1.6 \times 10^{-3}$ and less than $k = -6.4 \times 10^{-3}$. A weak flapping region is located in the region $-6.4 \times 10^{-3} \leq k \leq 1.6 \times 10^{-3}$. The hairy coating with a stiff base and flexible trailing edge is more beneficial to maintaining a stable shape, which is why the favourable drag zone is mainly located in the region of negative k. For the decreasing phase of k ($0 \geq k \geq -6.4 \times 10^{-3}$), the trailing edge of the hairy coating bends inward because of the more flexible trailing edge, resulting in the decrease of $\bar{A}$. The value of $\bar{E}_k$ remains unchanged because of the stiffer base. As k decreases further to -8×10^{-3}, the active flapping with significantly increased $\bar{A}$ and $\bar{E}_k$ induces a substantial increase in drag (figure 14*b*). As for the increasing phase of k ($0 \leq k \leq 8 \times 10^{-3}$), $\bar{A}$ and $\bar{E}_k$ increase rapidly with increasing k because of the more flexible base.

Note that a weak flapping case ($k = 4.8 \times 10^{-3}$) is observed in the active flapping region in figure 15(*b*). The contours of ω_z for $k = 0$ and $k = 4.8 \times 10^{-3}$ are shown in figure 16. A cone-shaped hairy coating with a flexible base is squeezed by the surrounding flow,

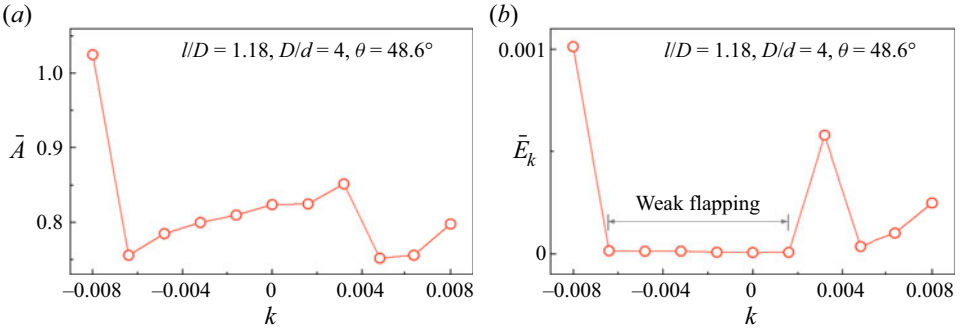

Figure 15. (*a*) Values of $\bar{A}$ and (*b*) $\bar{E}_k$ as functions of k for $l/D = 1.18$ ($D/d = 4$ and $\theta = 48.6°$).

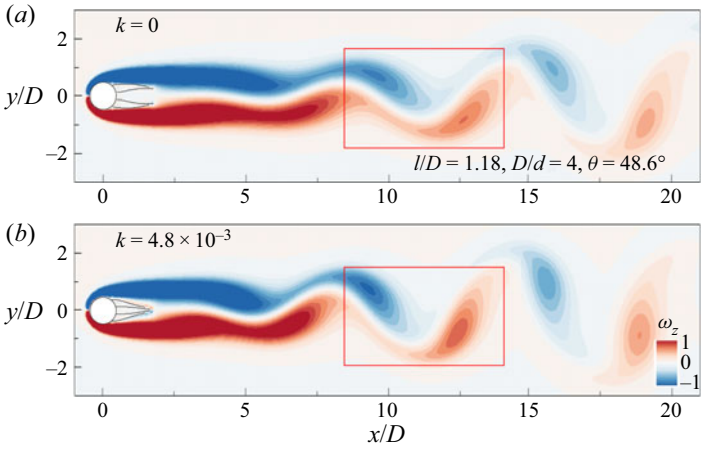

Figure 16. Contours of ω_z for different k ($D/d = 4$ and $\theta = 48.6°$): (*a*) $k = 0$ and (*b*) $k = 4.8 \times 10^{-3}$.

resulting in a minimum $\bar{A}$ at $k = 4.8 \times 10^{-3}$. As previously mentioned, a hairy coating with a width similar to that of the recirculation zone delays the vortex formation and stabilizes the wake. The role of the cone-shaped hairy coating with a much smaller width is weakened, resulting in enhanced ω_z in figure 16, which in turn leads to increased drag.

4. Conclusions

A two-dimensional flexible hairy coating attached to a cylinder was found to effectively reduce drag. In the present work, flow past such a cylinder–hair system was solved by the penalty IB method at a Reynolds number of 100, in an effort to reveal the hydrodynamic mechanism of drag reduction. The variation of drag was examined by varying the length (l), bending rigidity (γ), coating density (D/d) and coating angle (θ), showing a good agreement with the experimental data reported by Niu & Hu (2011). A maximum drag reduction of 22% was attained at a particular hairy coating condition. A transition of the shape deformation from the 'weak flapping regime' to the 'active flapping regime' was observed. A stable streamline shape of the hairy coating that delays the vortex formation and stabilizes the recirculation zone was identified. This shape increases the pressure near the rear surface of the cylinder, resulting in decreased form drag. Active flapping of the hairy coating with enhanced vortex shedding is adverse to drag reduction. The interaction

between multiple flexible filaments at a particular l/D and θ is beneficial to maintaining a stable streamline shape of the hairy coating; excessively small or large values of l/D and θ induce flapping. The stability of the hairy coating increases (i.e. the averaged flapping amplitude ($\bar{A}$) and kinetic energy ($\bar{E}_k$) decrease) with increasing γ and D/d until the critical point due to the interaction between multiple filaments is reached; $\bar{A}$ and $\bar{E}_k$ are insensitive to γ and D/d beyond the critical point. The effect of Re on drag reduction is insignificant when $Re \geq 100$. In addition, the hairy coating with a stiff base and flexible trailing edge is more beneficial to maintaining a stable streamline shape, leading to lower drag. Our investigation of the hydrodynamics of the basic configurations of a flexible hairy coating provides important insights into the hydrodynamic mechanism of drag reduction by a flexible hairy coating.

Funding. This study was supported by a grant from the National Research Foundation of Korea (No. 2020R1A2C2008106) and by a fund from the China Scholarship Council (No. 202006230245).

Declaration of interests. The authors report no conflict of interest.

Author ORCIDs.
Yingzheng Liu http://orcid.org/0000-0002-1480-921X;
Hyung Jin Sung http://orcid.org/0000-0002-4671-3626.

References

Abdi, R., Rezazadeh, N. & Abdi, M. 2019 Investigation of passive oscillations of flexible splitter plates attached to a circular cylinder. *J. Fluid Struct.* **84**, 302–317.

Assi, G.R., Bearman, P.W. & Kitney, N. 2009 Low drag solutions for suppressing vortex-induced vibration of circular cylinders. *J. Fluid Struct.* **25**, 666–675.

Bagheri, S., Mazzino, A. & Bottaro, A. 2012 Spontaneous symmetry breaking of a hinged flapping filament generates lift. *Phys. Rev. Lett.* **109**, 154502.

Banerjee, A., Gurugubelli, P.S., Kumar, N. & Jaiman, R.K. 2021 Influence of flexible fins on vortex-induced load over a circular cylinder at low Reynolds number. *Phys. Fluids* **33**, 113602.

Bechert, D.W., Bruse, M., Hage, W. & Meyer, R. 2000 Fluid mechanics of biological surfaces and their technological application. *Naturwissenschaften* **87**, 157–171.

Chen, Y., Ryu, J., Liu, Y. & Sung, H.J. 2020 Flapping dynamics of vertically clamped three-dimensional flexible flags in a Poiseuille flow. *Phys. Fluids* **32**, 071905.

De Langre, E. 2008 Effects of wind on plants. *Annu. Rev. Fluid Mech.* **40**, 141–168.

Deng, J., Mao, X. & Xie, F. 2019 Dynamics of two-dimensional flow around a circular cylinder with flexible filaments attached. *Phys. Rev.* E **100**, 053107.

Fage, A. & Johansen, F.C. 1928 XLII. The structure of vortex sheets. *Lond. Edin. Dublin Phil. Mag. J. Sci.* **5**, 417–441.

Favier, J., Dauptain, A., Basso, D. & Bottaro, A. 2009 Passive separation control using a self-adaptive hairy coating. *J. Fluid Mech.* **627**, 451–483.

García-Baena, C., Jiménez-González, J.I., Gutiérrez-Montes, C. & Martínez-Bazán, C. 2021 Numerical analysis of the flow-induced vibrations in the laminar wake behind a blunt body with rear flexible cavities. *J. Fluid Struct.* **100**, 103194.

Goldstein, D., Handler, R. & Sirovich, L. 1993 Modeling a no-slip flow boundary with an external force field. *J. Comput. Phys.* **105**, 354–366.

Glowinski, R., Pan, T.W., Hesla, T.I. & Joseph, D.D. 1999 A distributed Lagrange multiplier/fictitious domain method for particulate flows. *Intl J. Multiphase Flow* **25**, 755–794.

Huang, W.X., Shin, S.J. & Sung, H.J. 2007 Simulation of flexible filaments in a uniform flow by the immersed boundary method. *J. Comput. Phys.* **226**, 2206–2228.

Huang, W.X. & Sung, H.J. 2010 Three-dimensional simulation of a flapping flag in a uniform flow. *J. Fluid Mech.* **653**, 301–336.

Hwang, J., Lee, J., Sung, H.J. & Zaki, T.A. 2016 Inner–outer interactions of large-scale structures in turbulent channel flow. *J. Fluid Mech.* **790**, 128–157.

Hwang, J. & Sung, H.J. 2018 Wall-attached structures of velocity fluctuations in a turbulent boundary layer. *J. Fluid Mech.* **856**, 958–983.

KOEHL, M.A.R. 1984 How do benthic organisms withstand moving water? *Am. Zool.* **24**, 57–70.
KUNZE, S. & BRÜCKER, C. 2012 Control of vortex shedding on a circular cylinder using self-adaptive hairy-flaps. *C. R. Méc.* **340**, 41–56.
LEE, J., LEE, J.H., CHOI, J.-I. & SUNG, H.J. 2014 Spatial organization of large- and very-large-scale motions in a turbulent channel flow. *J. Fluid Mech.* **749**, 818–840.
LEE, J. & YOU, D. 2013 Study of vortex-shedding-induced vibration of a flexible splitter plate behind a cylinder. *Phys. Fluids* **25**, 110811.
MAO, Q.A., ZHAO, J., LIU, Y. & SUNG, H.J. 2021*a* Drag reduction by a flexible afterbody. *Phys. Fluids* **33**, 122009.
MAO, Q.A., WANG, P., HE, C. & LIU, Y. 2021*b* Unsteady flow structures behind a shark denticle replica on the wall: Time-resolved particle image velocimetry measurements. *Phys. Fluids* **33**, 075109.
NIU, J. & HU, D.L. 2011 Drag reduction of a hairy disk. *Phys. Fluids* **23**, 101701.
PARK, T.S. & SUNG, H.J. 2001 Development of a near-wall turbulence model and application to jet impinging heat transfer. *Intl J. Heat Fluid Flow* **22** (10), 18.
PASTOOR, M., HENNING, L., NOACK, B.R., KING, R. & TADMOR, G. 2008 Feedback shear layer control for bluff body drag reduction. *J. Fluid Mech.* **608**, 161–196.
PESKIN, C.S. 2002 The immersed boundary method. *Acta Numerica* **11**, 479–517.
ROSHKO, A. 1955 On the wake and drag of bluff bodies. *J. Aeronaut. Sci.* **22**, 124–132.
SHEN, P., LIN, L., WEI, Y., DOU, H. & TU, C. 2019 Vortex shedding characteristics around a circular cylinder with flexible film. *Eur. J. Mech. (*B*/Fluid)* **77**, 201–210.
SHIN, S.J., HUANG, W.X. & SUNG, H.J. 2008 Assessment of regularized delta functions and feedback forcing schemes for an immersed boundary method. *Intl J. Numer. Meth. Fluids* **58**, 263–286.
SHUKLA, S., GOVARDHAN, R.N. & ARAKERI, J.H. 2013 Dynamics of a flexible splitter plate in the wake of a circular cylinder. *J. Fluid Struct.* **41**, 127–134.
TEKSIN, S. & YAYLA, S. 2016 Effects of flexible splitter plate in the wake of a cylindrical body. *J. Appl. Fluid Mech.* **9**, 3053–3059.
WILLIAMSON, C.H. & GOVARDHAN, R. 2004 Vortex-induced vibrations. *Annu. Rev. Fluid Mech.* **36**, 413–455.
WU, J., QIU, Y.L., SHU, C. & ZHAO, N. 2014 Flow control of a circular cylinder by using an attached flexible filament. *Phys. Fluids* **26**, 103601.
WU, J., WU, J. & ZHAN, J. 2016 Characteristics of flow over a circular cylinder with two attached filaments. *J. Fluid Struct.* **66**, 269–281.
XU, S. & WANG, Z.J. 2006 An immersed interface method for simulating the interaction of a fluid with moving boundaries. *J. Comput. Phys.* **216**, 454–493.
YUAN, H.Z., NIU, X.D., SHU, S., LI, M. & YAMAGUCHI, H. 2014 A momentum exchange-based immersed boundary-lattice Boltzmann method for simulating a flexible filament in an incompressible flow. *Comput. Maths Applics.* **67**, 1039–1056.